ЖЭТФ, 2015, том 148, вып. 4 (10), стр. 706–713

Fe AND Co NANOSTRUCTURES EMBEDDED INTO THE Cu(100) SURFACE: SELF-ORGANIZATION AND MAGNETIC PROPERTIES

S. V. Kolesnikov**, A. L. Klavsyuk, A. M. Saletsky

Faculty of Physics, Lomonosov Moscow State University
119991, Moscow, Russian Federation

Received March 11, 2015

The self-organization and magnetic properties of small iron and cobalt nanostructures embedded into the first layer of a Cu(100) surface are investigated using the self-learning kinetic Monte Carlo method and density functional theory. The similarities and differences between the Fe/Cu(100) and the Co/Cu(100) are underlined. The time evolution of magnetic properties of a copper monolayer with embedded magnetic atoms at 380 K is discussed.

DOI: 10.7868/S0044451015100077

1. INTRODUCTION

Studies of magnetic nanostructures play a key role in high-density memory storage and the development of nano-electronics. Nanostructures from magnetic $3d$ metals are very appealing because of their unusual physical properties. The epitaxial growth of Fe [1, 2], Co [3, 4], and Ni [5] thin films on a Cu(100) surface has been investigated. Magnetic properties of Fe [2, 6], Co [7, 8], and Ni [5] thin films were investigated experimentally. Interesting magnetic properties of nanowires [9–12] and nanoclusters [13–15] have also been found recently. However, small supported nanostructures can be unstable at room temperature. This motivates the investigation of embedded nanostructures.

The mobility of embedded atoms was investigated with the use of a scanning tunnel microscopy (STM) [16–20]. Surface vacancies were shown to be responsible for the mobility of embedded Mn [16], Pd [17], In [18], and Co [19, 20] atoms in the first layer of a Cu(100) surface. The experiments of Kurnosikov et al. [19] showed that single atoms of Co embedded into the Cu(100) surface can be manipulated with the STM tip and small atomic chains stable at the room temperature can be created in a controlled way. The similarity of the Co/Cu(100) and Fe/Cu(100) epitaxial systems suggests that the diffusion of embedded Fe atoms also leads to the formation of small nanostructures.

The main goal of this paper is to compare the self-organization and magnetic properties of small Fe and Co nanostructures embedded into a Cu(100) surface. It is also interesting to discuss the time evolution of magnetic properties of a copper monolayer with embedded magnetic atoms.

This paper is organized as follows. In Sec. 2, we present our kinetic Monte Carlo (kMC) method and describe the technique of calculation of magnetic properties of nanostructures. In Sec. 3, the results of the kMC simulations of surface morphology and the magnetic properties of the surface are discussed. Finally, Sec. 4 summarizes our results.

2. COMPUTATIONAL METHOD

For a realistic simulation of the motion of embedded atoms, the self-learning kinetic Monte Carlo method (SLkMC) [21] is applied. The original SLkMC method can be modified [22, 23] for heterogeneous systems such as Fe/Cu(100) or Co/Cu(100), where simple events are the most important and complex concerted atomic motions occur rarely, and their influence on the evolution of the system can be neglected. In this model, the diffusion of embedded atoms and dimers only through exchanges with surface vacancies is considered. The concentration of vacancies is not high; hence, to accelerate the SLkMC calculations, it is supposed that only surface vacancies can move. Three types of va-

*E-mail: kolesnikov@physics.msu.ru

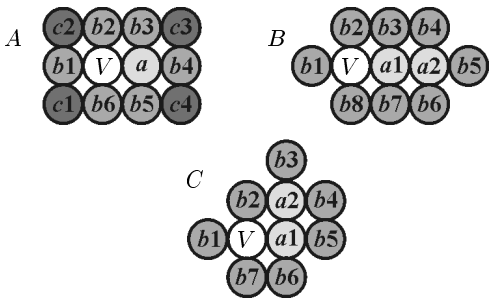

Fig. 1. Local environments for a vacancy transition to the first-nearest-neighbor position, the second-nearest-neighbor position, and the third-nearest-neighbor position in the first layer of the (100) surface are presented in respective schemes (A), (C), and (B). In (A), the atom jumps from position a to position V. In the cases (B) and (C), the first atom jumps from position $a1$ to position V and the second atom jumps from position $a2$ to position $a1$. The nearest-neighbor positions of the vacancy and the moving atoms are denoted as $b1$–$b8$; and $c1$–$c4$ are the second-nearest-neighbor positions

cancy transitions are considered (see Fig. 1): (a) jumps into the first-nearest-neighbor positions are equivalent to single copper or impurity atom jumps; (b) jumps into the second-nearest-neighbor positions are equivalent to rotations of copper–copper, copper–impurity, or impurity–impurity dimers; and (c) jumps into the third-nearest-neighbor positions are equivalent to shifts of the dimers. The maximum number of events in the presented model is

$$2 \cdot 3^{10} + 2^2 \cdot 3^8 + 2^2 \cdot 3^7 = 153090$$

(without considering the symmetry). The initial configuration is a random homogenous distribution of impurity atoms and vacancies in the first layer of the Cu(100) surface. This assumption is valid in the case of a low deposition flux [22].

The barriers are computed "on the fly" by the nudged elastic band (NEB) method [24] incorporated into the kMC algorithm. To calculate the diffusion barriers, the interatomic potentials formulated in the second moment of the tight-binding approximation [25, 26] are used. In this approximation, the attractive term E_B^i (band energy) contains the many-body interaction. The repulsive part E_R^i is described by pair interactions (the Born–Mayer form). The cohesive energy E_C is the sum of the band energy and the repulsive part:

$$E_C = \sum_i \left(E_R^i + E_B^i\right), \qquad (1)$$

$$E_B^i = -\left\{\sum_j \xi_{\alpha\beta}^2 \exp\left[-2q_{\alpha\beta}\left(\frac{r_{ij}}{r_0^{\alpha\beta}} - 1\right)\right]\right\}^{1/2}, \qquad (2)$$

$$E_R^i = \sum_j \left[A_{\alpha\beta}^1\left(\frac{r_{ij}}{r_0^{\alpha\beta}} - 1\right) + A_{\alpha\beta}^0\right] \times \exp\left[-p_{\alpha\beta}\left(\frac{r_{ij}}{r_0^{\alpha\beta}} - 1\right)\right], \qquad (3)$$

where r_{ij} is the distance between atoms i and j; α and β are types of atoms; $\xi_{\alpha\beta}$ is an effective hopping integral; $p_{\alpha\beta}$ and $q_{\alpha\beta}$ describe the decay of the interaction strength with the distance between atoms; and $r_0^{\alpha\beta}$, $A_{\alpha\beta}^0$, and $A_{\alpha\beta}^1$ are adjustable parameters of the interatomic interaction. The interatomic potentials reproduce the bulk properties of Cu, Fe, and Co crystals and the *ab initio* calculated properties of the supported and embedded Co and Fe clusters. The details of the fitting procedure are described in [26]. The parameters of the potentials are taken from the literature [27, 28] and are presented in Table 1.

The positions of impurity and copper atoms are determined in a fully relaxed geometry. The slab used to calculate the barriers consists of eight layers with 2000 atoms per layer. The two bottom layers are fixed, and periodic boundary conditions are applied to the surface plane. The cutoff radius for the interatomic potentials is set to 6.0 Å. Different prefactors are taken for the diffusion of adatoms (first type of vacancy transitions) and dimers (second and third types of vacancy transitions): $\nu_{ad}^0 = 15$ THz and $\nu_{dim}^0 = 300$ THz. These values are typical for jumps and exchanges of atoms on the Cu(100) surface [29, 30]. The random number generator from book [31] is used to improve the accuracy of the calculations.

Ab initio density functional theory (DFT) calculations of the spin and orbital magnetic moments and of the magnetic anisotropy energy (MAE) of Fe and Co nanostructures embedded into the Cu(100) surface were performed using the projector augmented-wave (PAW) technique [32, 33] implemented in the Vienna *ab initio* simulation package (VASP) [34]. The calculations are based on the DFT with the generalized gradient approximation (GGA) [35, 36]. We used the same methodology as in previous calculations of the magnetic anisotropy of Co and Fe adatoms and ultrathin films on Rh(111) and Pt(111) substrates [37, 38]. The substrate was modeled as periodically repeated slabs consisting of up to six atomic layers separated by a sufficiently thick vacuum space of 16 Å. At this slab

Table 1. Parameters of interatomic potentials [27, 28]

Parameter	Cu–Cu	Fe–Fe	Co–Co	Fe–Cu	Co–Cu
A^1, eV	0.0	−0.777	0.0	−1.909	−1.552
A^0, eV	0.086	0.162	0.121	−0.026	−0.037
ξ, eV	1.224	1.573	1.579	0.881	0.852
p	10.939	5.872	11.391	7.148	7.623
q	2.280	2.105	2.350	5.178	5.518
r_0, Å	2.556	2.474	2.495	2.441	2.500

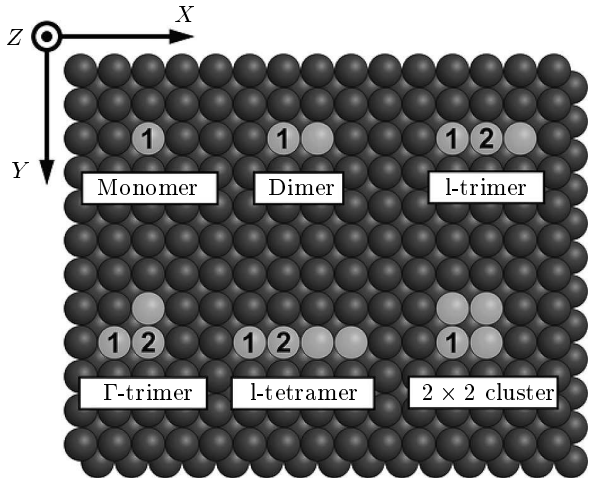

Fig. 2. Schematic view of nanostructures embedded in a surface. Dark- and light-gray balls respectively represent Cu and impurity (Co or Fe) atoms

thickness, the induced moments on the lower surface are nearly zero (a node in the oscillatory decaying moments falls close to the surface) and hence no artificially enhanced moment exists at the lower surface. A 6×4 surface unit cell was used for the l-tetramer and 5×5 surface unit cells for all other nanostructures (see Fig. 2). The coordinates of impurity nanostructures and the positions of copper atoms in the three topmost layers of the substrate were optimized using scalar relativistic calculations until the forces on all unconstrained atoms converged to less than 0.01 eV/Å. The geometry and electronic and magnetic ground states resulting from the scalar relativistic calculation were used to initialize relativistic calculations including the spin–orbit coupling. Recent work [39] demonstrated that the relaxations of Fe and Co adatoms on Pt(111) with and without the spin–orbit coupling are almost identical. A cutoff energy of 250 eV is used.

The MAE is calculated as the total energy difference between the two relativistic band structure calculations for two different magnetization directions using the frozen charge density obtained in a previous self-consistent scalar relativistic calculation [40].

The calculations including the spin–orbit coupling require a fine k-point mesh for the Brillouin-zone integrations. Test calculations were performed for Fe and Co monomers in a Cu(100) surface for three different k-point grids: $3 \times 3 \times 1$, $5 \times 5 \times 1$, and $12 \times 12 \times 1$ for a 3×3 surface unit cell and $3 \times 3 \times 1$, $5 \times 5 \times 1$, and $7 \times 7 \times 1$ for a 5×5 surface unit cell generated by the Monkhorst–Pack scheme [41] in conjunction with the Fermi–Dirac smearing method. The $5 \times 5 \times 1$ grid provided the best compromise between accuracy and computational effort.

3. RESULTS AND DISCUSSIONS

In this section, we present the investigation of the self-organization of Fe and Co nanostructures embedded in the first layer of a Cu(100) surface. We next discuss, magnetic properties of the most widespread nanostructures.

3.1. SLkMC investigation

The diffusion of embedded Fe and Co atoms in a Cu(100) surface at 300–400 K can be mainly realized via respective Fe-vacancy and Co-vacancy exchanges [42, 43]. This assumption is in good agreement with the experimental results in [19, 20]. The only mechanism of diffusion of embedded impurity atoms (Fe or Co) is as follows: the surface vacancy jumps toward an impurity atom, replaces it, and goes away. A surface vacancy can diffuse in a clean Cu(100) surface in two different ways (see Table 2): the vacancy can move the nearest-neighbor distance (a single jump of a Cu atom)

with a barrier of 0.38 eV, or the third-neighbor distance (a shift of a Cu–Cu dimer) with a barrier of 0.54 eV. Another possibility of vacancy transitions is the rotation of a Cu–Cu dimer, but this event is separated into two successive single jumps of Cu atoms. Such events are no longer independent and are disregarded in the calculations.

Table 2 shows that the diffusion of an impurity atom or the association of an impurity–impurity dimer can be realized in three different ways: the jump of a single impurity atom, the shift of an impurity–Cu dimer, and the shift of a Cu–impurity dimer. These examples illustrate the general features of the Fe/Cu(100) and Co/Cu(100) systems. First, barriers for the shifts of dimers are usually higher than barriers for the single jumps of atoms. However, the shifts of dimers have a higher frequency prefactor, and therefore play a very important role in the formation of nanostructures at 300–400 K [23]. Second, rotations of dimers occur very rarely and do not influence the formation of embedded nanostructures. Third, the analogous barriers for both systems are very close, but not equal. The last fact leads to some interesting differences in the time evolution of Fe/Cu(100) and Co/Cu(100) systems.

Figure 3 shows the results of our SLkMC investigations of the self-organization of Fe and Co embedded nanostructures at 380 K. The relative populations of the simplest embedded Co nanostructures are shown on a logarithmic scale. In the first layer of the (100) surface, the following types of the simplest nanostructures can be formed: (i) dimers; (ii) two types of trimers: l- and Γ-trimers (see Fig. 1); and (iii) five types of tetramers. Of these eight types of nanostructures, only the 2×2 cluster is actually compact; the other structures are noncompact atomic chains. The frequency of the dissociation of 2×2 clusters is close to zero at 380 K. Hence, the number of 2×2 clusters characterizes the total number of compact embedded nanostructures. The full time evolution of the embedded Co nanostructures can be divided into three stages: (I) monomer domination, (II) chain domination, and (III) cluster domination. The monomer domination stage is characterized by a decrease in the monomer population and intensive formation of noncompact chains. Compact nanostructures are almost completely absent at this stage. In the chain domination stage, the number of monomers decreases. The number of chains remains constant at the beginning of the stage and begins to decrease toward the end. The number of compact embedded structures grows monotonically. In the cluster domination stage, the number of all noncompact structures drops to zero and the number of compact structures tends to a constant value. Beyond this point, the surface morphology does not change on any reasonable timescale.

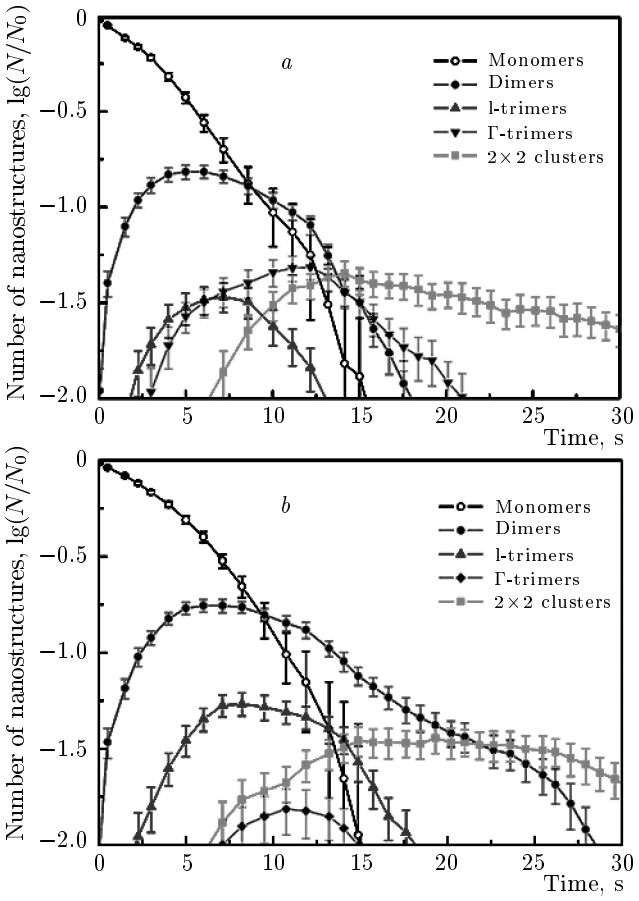

Fig. 3. The time evolution of the population of the simplest (a) Fe and (b) Co nanostructures at $T = 380$ K. The concentrations of the embedded impurity adatoms and the vacancies are $n_{ad} = 0.1$ ML and $n_{vac} = 0.0023$ ML; $N_0 = 1000$ is the initial number of impurity monomers. The average numbers of nanostructures are presented along with the sample standard deviations

There are two main differences in the self-organization of Fe and Co embedded nanostructures. First, the number of dimers in the Fe/Cu(100) system decreases twice as fast as in the Co/Cu(100) system. Second, the number of linear Co chains (l-trimers and l-tetramers) is higher than the number of Γ-trimers at the chain domination stage. At the same time, the number of angle nanostructures is higher in the Fe/Cu(100) system, while the number of linear chains is very low. These features can be explained at the atomic level in the following way. On one hand, the formation of Γ-trimers is more energetically preferable than the formation of l-trimers in both systems. But the difference between

Table 2. Activation barriers for basic atomic processes in electronvolts. Single jumps of atoms are labeled as (a)–$(b1)(b2)(b3)(b4)(b5)(b6)$–$(c1)(c2)(c3)(c4)$ and shifts of dimers are labeled as $(a1)(a2)$–$(b1)(b2)(b3)(b4)(b5)(b6)(b7)(b8)$ (see Fig. 1); 0 = Cu, 1 = vacancy, 2 = Co

Atomic process	Type of transition	Label of transition	Fe	Co
Diffusion of free vacancy	single jump	0–000000–0000	0.38	0.38
	shift of dimer	00–00000000	0.54	0.54
Diffusion of impurity atom	single jump	2–000000–0000	0.59	0.61
	shift of dimer	20–00000000	0.65	0.68
	shift of dimer	02–00000000	0.77	0.78
Association of dimer	single jump	2–000002–0000	0.34	0.31
	shift of dimer	20–00000002	0.43	0.42
	shift of dimer	02–00000020	0.57	0.52

Table 3. Average MAE ΔE for small embedded nanostructures in a Cu(100) surface calculated for the magnetization switch from the normal Z towards the in-plane X and Y directions, as shown in Fig. 2. Negative MAE values indicate a preferred in-plane magnetization. All values are in meV/atom

Structure	$\Delta E_{\mathrm{Fe}}(X,Z)$	$\Delta E_{\mathrm{Fe}}(Y,Z)$	$\Delta E_{\mathrm{Co}}(X,Z)$	$\Delta E_{\mathrm{Co}}(Y,Z)$
monomer	−0.11	−0.11	−2.01	−2.01
dimer	0.14	0.10	−1.71	−1.11
l-trimer	0.06	0.04	−1.59	−0.94
Γ-trimer	0.03	0.03	−0.96	−0.96
l-tetramer	0.05	0.03	−1.68	−1.09
2×2 cluster	0.02	0.02	−0.36	−0.36

the binding energies $E^{bind}_{l\text{-}trimer} - E^{bind}_{\Gamma\text{-}trimer}$ is higher in the Fe/Cu(100) system than in the Co/Cu(100) system: 0.104 and 0.090 eV, respectively. On the other hand, the processes of dissociation of linear chains are faster in the Fe/Cu(100) system. Indeed, the most probable way of dissociation of a dimer (and other linear structures) is realized via the shift of the impurity–Cu dimer (the event 20-00000020; see caption to Table 2). This shift of the dimer has a barrier of 0.64 eV in the Fe/Cu(100) system and 0.71 eV in the Co/Cu(100) system.

It is necessary to mention that the self-organization time significantly depends on the concentration of surface vacancies. In the present case, the only source of surface vacancies is a small vacancy cluster, which is formed from the free vacancies in a simulation cell. However, various defects of the surface can be the sources of vacancies in real experiments. The concentration of surface vacancies can also increase in the process of scanning the surface with STM [44, 45]. Consequently, the experimental self-organization time of embedded nanostructures can be significantly different from the presented in Figs. 3 and 4.

3.2. Magnetic anisotropy energies, and spin and orbital moments

The magnetic anisotropy energy $\Delta E(I,Z)$ (where $I = X, Y$) was calculated as the difference of total energies of all atoms in the calculation cell in the cases where the magnetic moments of impurity atoms (Fe or Co) were respectively oriented along the I and Z axes. The X, Y, and Z directions are shown in Fig. 2. A positive MAE value $\Delta E(I,Z)$ means that the magnetization of impurity atoms along the Z axis is more energetically favorable, whereas a negative value corresponds to the preferable I axis.

Table 4. Calculated spin magnetic moments M and orbital magnetic moments L for X, Y, and Z magnetization orientations for Fe and Co atoms in embedded nanostructures (see Fig. 2). All values are in μ_B

Structure	Position	M^{Fe}	L_X^{Fe}	L_Y^{Fe}	L_Z^{Fe}	M^{Co}	L_X^{Co}	L_Y^{Co}	L_Z^{Co}
monomer	1	2.73	0.24	0.24	0.22	1.71	0.65	0.65	0.55
dimer	1	2.84	0.09	0.10	0.10	1.77	0.38	0.24	0.19
l-trimer	1	2.91	0.12	0.11	0.11	1.75	0.40	0.23	0.20
	2	2.87	0.08	0.09	0.08	1.76	0.16	0.11	0.12
Γ-trimer	1	2.90	0.10	0.11	0.12	1.80	0.36	0.26	0.20
	2	2.73	0.09	0.09	0.12	1.84	0.20	0.20	0.13
l-tetramer	1	2.91	0.12	0.11	0.11	1.75	0.42	0.23	0.19
	2	2.87	0.09	0.08	0.08	1.76	0.18	0.09	0.10
2×2 cluster	1	2.80	0.10	0.10	0.10	1.81	0.24	0.24	0.19

The average MAE for the embedded clusters are listed in Table 3. The noncompact nanostructures have a higher MAE than the compact ones. The reason for such a tendency is the interactions between impurity atoms (Co–Co or Fe–Fe), leading to a decrease in the MAE of individual atoms. As the result, the outer atoms, having a smaller number of nearest neighbors, contribute much more to the average MAE than the inner atoms do. The average MAE of Co nanostructures is much higher than the average MAE of similar nanostructures with Fe atoms. Moreover, these nanostructures are characterized by different directions of the easy magnetization axes. An in-plane magnetization is exhibited in all Co clusters, but Fe nanostructures (except monomers) have an out-of-plane magnetization. Comparing the calculated MAE with the results obtained earlier [9, 14], we emphasize the important role of surface relaxation in copper [46].

Calculations of the spin and orbital magnetic moments for monomers and selected embedded nanostructures are presented in Table 4, where the positional indices in the nanostructures refer to the corresponding numbers in Fig. 2. The spin magnetic moment of Fe atoms is about a factor of 1.5 higher than that of Co atoms. The spin magnetic moment of the monomer is lower than the spin moments of the small embedded nanostructures. The general tendency of increasing spin magnetic moments with increasing the number of the neighboring Co atoms can be explained by the fact that the d–d interaction in the embedded nanostructures extends the d-states and, consequently, the spin magnetic moment increases [14]. The values presented in Table 4 are in good agreement with the results reported in the literature [9, 14]. The spin magnetic moment anisotropy of atoms of $3d$ metals for different magnetisation orientations is negligible [37].

In contrast to the spin magnetic moments, the orbital magnetic moment anisotropy is fairly large, because in the transition metals with a more-than-half-filled d band, the largest orbital magnetic moment is found along the easy magnetization direction favored by the MAE [47]. Similar to MAE, the orbital magnetic moments of small embedded nanostructures are decreased drastically by interactions between impurity atoms. Finally, the surface relaxation leads to a substantial decrease in the orbital magnetic moments of the embedded Fe and Co atoms [14, 46].

3.3. The time evolution of magnetic properties

Combining the results presented above, it is easy to calculate the time evolution of the magnetic properties of the Cu(100) surface with embedded Fe and Co nanostructures. For example, we have calculated the time evolution of the average MAE of Cu(100) monolayer (see Fig. 4). Here, we used the data presented in Fig. 3 and Table 3, and the assumption that all large nanostructures are compact and have the same MAE per atom as a 2×2 cluster. Figure 4 shows a monotonic decrease in the average MAE of the copper monolayer with embedded Co atoms from 2.01 to 0.360 meV per Co atom. In the case of the Fe/Cu(100) system, the average MAE of the monolayer exhibits a more complex nonmonotonic behavior with rotation of the easy magnetization axes.

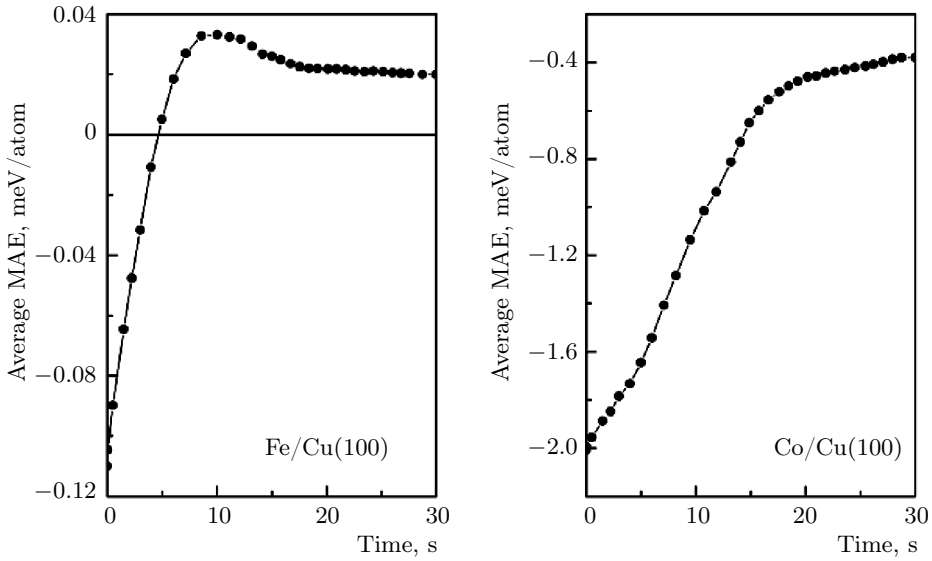

Fig. 4. The time evolution of the average MAE (per impurity atom) of a Cu(100) monolayer with embedded Fe or Co atoms at $T = 380$ K

4. CONCLUSION

Using our SLkMC method, we have investigated the self-organization of Fe and Co nanostructures in the first layer of the Cu(100) surface at 380 K. The time evolution passes through three stages: (I) monomer domination, (II) chain domination, and (III) cluster domination. Formation of embedded nanostructures in the Fe/Cu(100) and the Co/Cu(100) systems is similar in the initial and final stages, but it has some differences in the chain-domination stage. Co atoms have a tendency to form short linear chains. At the same time, angular Fe chains are more preferable than linear chains. This picture of self-organization weakly depends on the concentration of impurity atoms in the range 0.05–0.15 ML, and it is valid in the temperature range 350–400 K.

Our DFT calculations show that the MAE of embedded Co atoms is significantly higher than the MAE of Fe atoms in analogous nanostructures. At the same time, similar Fe and Co nanostructures (except monomers) have different directions of the easy magnetization axes. The spin magnetic moments of the embedded Fe atoms are about a factor of 1.5 higher than those for Co atoms. On the other hand, the orbital magnetic moments of Co atoms are several times higher than those for Fe atoms. The interaction between impurity atoms leads to an increase in the spin magnetic moments and to a decrease in MAE and orbital magnetic moments. We also emphasize the critical role of the surface relaxation in the calculation of the MAE of embedded nanostructures.

Figure 4 illustrates that the magnetic properties of the Cu(100) surface with embedded Fe or Co atoms dramatically change in the course of time evolution. This fact provides an opportunity to create surfaces with prescribed magnetic properties. Therefore, our investigation will be helpful for future technical applications.

Computational resources were provided by the Research Computing Center, Moscow State University (MSU NIVC). This work was supported by RFBR (grant № 15-32-20560 mol-a-ved).

REFERENCES

1. J. Giergiel, J. Shen, J. Woltersdorf, A. Kirilyuk, and J. Kirschner, Phys. Rev. B **52**, 8528 (1995).

2. X. F. Jin, J. Phys. D: Appl. Phys. **35**, 2332 (2002).

3. U. Ramsperger, A. Vaterlaus, P. Pfäffli, U. Maier, and D. Pescia, Phys. Rev. B **53**, 8001 (1996).

4. R. Pentcheva, K. A. Fichthorn, M. Scheffler, T. Bernhard, R. Pfandzelter, and H. Winter, Phys. Rev. Lett. **90**, 076101 (2003).

5. C. L. Lin, A. W. Wu, Y. C. Wang, Y. C. Tseng, and J. S. Tsay, Phys. Chem. Chem. Phys. **15**, 2360 (2013).

6. M. Straub, R. Vollmer, and J. Kirschner, Phys. Rev. Lett. **77**, 743 (1996).

7. J. H. Dunn, D. Arvanitis, N. Martensson, M. Tischer, F. May, M. Russo, and K. Baberschke, J. Phys.: Cond. Matt. **7**, 1111 (1995).

8. C. C. Kuo, C. L. Chiu, W. C. Lin, and M. T. Lin, Surface Science **520**, 121 (2002).

9. B. Lazarovits, L. Szunyogh, P. Weinberger, and B. Újfalussy, Phys. Rev. B **68**, 024433 (2003).

10. F. Tian, Z. P. Huang, and L. Whitmore, Phys. Chem. Chem. Phys. **14**, 8537 (2012).

11. E. M. Smelova, K. M. Tsysar, and A. M. Saletsky, Phys. Chem. Chem. Phys. **16**, 8360 (2014).

12. N. Zaki, C. A. Marianetti, D. P. Acharya, P. Zahl, P. Sutter, J. Okamoto, P. D. Johnson, A. J. Millis, and R. M. Osgood, Phys. Rev. B **87**, 161406 (2013).

13. J. Izquierdo, A. Vega, and L. C. Balbás, Phys. Rev. B **55**, 445 (1997).

14. Š. Pick, V. S. Stepanyuk, A. L. Klavsyuk, L. Niebergall, W. Hergert, J. Kirschner, and P. Bruno, Phys. Rev. B **70**, 224419 (2004).

15. A. B. Klautau, L. M. Socolovsky, R. N. Nogueira, and H. M. Petrilli, J. Phys.: Cond. Matt. **21**, 506001 (2009).

16. T. Flores, S. Junghans, and M. Wuttig, Surface Science **371**, 1 (1997).

17. M. L. Grant, B. S. Swartzentruber, N. C. Bartelt, and J. B. Hannon, Phys. Rev. Lett. **86**, 4588 (2001).

18. R. van Gastel, E. Somfai, S. B. van Albada, W. van Saarloos, and J. W. M. Frenken, Phys. Rev. Lett. **86**, 1562 (2001).

19. O. Kurnosikov, J. T. Kohlhepp, and W. J. M. de Jonge, Europhys. Lett. **64**, 77 (2003).

20. R. van Gastel, R. van Moere, H. J. W. Zandvliet, and B. Poelsema, Surface Science **605**, 1956 (2011).

21. O. Trushin, A. Karim, A. Kara, and T. S. Rahman, Phys. Rev. B **72**, 115401 (2005).

22. S. V. Kolesnikov, A. L. Klavsyuk, and A. M. Saletsky, Surface Science **612**, 48 (2013).

23. S. V. Kolesnikov, A. L. Klavsyuk, and A. M. Saletsky, Europ. Phys. J. B **86**, 399 (2013).

24. H. Jónsson, G. Mills, and K. W. Jacobsen, *Nudged Elastic Band Method for Finding Minimum Energy Paths of Transitions*, World Scientific (1998), Ch. 16, p. 385.

25. F. Cleri and V. Rosato, Phys. Rev. B **48**, 22 (1993).

26. N. A. Levanov, V. S. Stepanyuk, W. Hergert, D. I. Bazhanov, P. H. Dederichs, A. Katsnelson, and C. Massobrio, Phys. Rev. B **61**, 2230 (2000).

27. N. N. Negulyaev, V. S. Stepanyuk, W. Hergert, P. Bruno, and J. Kirschner, Phys. Rev. B **77**, 085430 (2008).

28. N. N. Negulyaev, V. S. Stepanyuk, P. Bruno, L. Diekhöner, P. Wahl, and K. Kern, Phys. Rev. B **77**, 125437 (2008).

29. G. Boisvert and L. J. Lewis, Phys. Rev. B **56**, 7643 (1997).

30. S. A. Dokukin, O. V. Drozdov, S. V. Kolesnikov, and A. M. Saletsky, Phys. Sol. St. **55**, 1505 (2013).

31. *Numerical Recipes in Fortran90*, http://www.nrbook.com/a/bookf90pdf.php (1996).

32. P. E. Blöchl, Phys. Rev. B **50**, 17953 (1994).

33. G. Kresse and D. Joubert, Phys. Rev. B **59**, 1758 (1999).

34. G. Kresse and J. Hafner, Phys. Rev. B **48**, 13115 (1993).

35. Y. Wang and J. P. Perdew, Phys. Rev. B **44**, 13298 (1991).

36. J. P. Perdew and Y. Wang, Phys. Rev. B **45**, 13244 (1992).

37. P. Błoński, A. Lehnert, S. Dennler, S. Rusponi, M. Etzkorn, G. Moulas, P. Bencok, P. Gambardella, H. Brune, and J. Hafner, Phys. Rev. B **81**, 104426 (2010).

38. A. Lehnert, S. Dennler, P. Błoński, S. Rusponi, M. Etzkorn, G. Moulas, P. Bencok, P. Gambardella, H. Brune, and J. Hafner, Phys. Rev. B **82**, 094409 (2010).

39. P. Blonski and J. Hafner, J. Phys.: Cond. Matt. **21**, 426001 (2009).

40. *The VASP guide*, http://cms.mpi.univie.ac.at/VASP/.

41. H. J. Monkhorst and J. D. Pack, Phys. Rev. B **13**, 5188 (1976).

42. S. V. Kolesnikov, A. L. Klavsyuk, and A. M. Saletsky, Phys. Rev. B **79**, 115433 (2009).

43. S. V. Kolesnikov, JETP Lett. **99**, 286 (2014).

44. S. V. Kolesnikov, A. L. Klavsyuk, and A. M. Saletsky, JETP Lett. **89**, 471 (2009).

45. S. V. Kolesnikov, A. L. Klavsyuk, and A. M. Saletsky, Phys. Rev. B **80**, 245412 (2009).

46. S. V. Kolesnikov, A. L. Klavsyuk, and A. M. Saletsky, JETP Lett. **99**, 646 (2014).

47. P. Bruno, Phys. Rev. B **39**, 865 (1989).